INTERNATIONAL JOURNAL FOR NUMERICAL METHODS IN FLUIDS
Int. J. Numer. Meth. Fluids 2006; **52**:355–379

LES of the compressed Taylor vortex flow using a finite volume/finite element method on unstructured grids

C. Le Ribault*,†, L. Le Penven‡ and M. Buffat§

Laboratoire de Mécanique des Fluides et d'Acoustique, UMR CNRS 5509, Ecole Centrale de Lyon, Université Claude Bernard Lyon I, 36, avenue Guy de Collongue, 69134 Ecully, France

SUMMARY

Large-eddy simulations (LES) have been performed of a compressed vortex flow undergoing transition to turbulence. The numerical method is based on a finite volume/finite element discretization of the compressible Navier–Stokes equations on unstructured grids and a Roe second-order scheme with MUSCL extrapolation. A particular attention is paid to the dissipative character of the method, controlled by a coefficient related to the upwind part of the numerical scheme, and its interference with the subgrid model. The accuracy of the method is first checked in the case of decaying homogeneous isotropic turbulence. The investigation is then directed to a plane Taylor vortex flow submitted to compression, in a direction perpendicular to the vorticity vector. This flow is unstable with respect to three-dimensional perturbations and transition to turbulence is observed if the Reynolds number is large enough. The numerical method is used to simulate this vortex flow for two values of the Reynolds number. For the lower value, the flow is unstable but remains laminar and no subgrid model is used. For the higher one, the turbulence appears and the standard and the dynamic Smagorinsky models are tested. The LES results are compared to those obtained by direct numerical simulations (DNS) using a spectral Fourier method. Copyright © 2006 John Wiley & Sons, Ltd.

KEY WORDS: LES; unstructured grids; compressed flows; Roe solver

1. INTRODUCTION

Large-eddy simulation (LES) is a method for turbulent flow simulation in which the large-scale motions are predicted by solving the low-pass filtered Navier–Stokes equations.

---

*Correspondence to: Catherine Le Ribault, Laboratoire de Mécanique des Fluides et d'Acoustique, UMR CNRS 5509, Ecole Centrale de Lyon, Université Claude Bernard Lyon I, 36, avenue Guy de Collongue, 69134 Ecully, France.
†E-mail: Catherine.Le-Ribault@ec-lyon.fr
‡E-mail: lionel.le-penven@ec-lyon.fr
§E-mail: marc.buffat@ec-lyon.fr

Contract/grant sponsor: CNRS
Contract/grant sponsor: PSA
Contract/grant sponsor: Renault

Received 12 January 2005
Revised 7 October 2005
Accepted 18 October 2005

Compared to methods based on the Reynolds-averaged Navier–Stokes (RANS) equations, which are still mostly employed for engineering applications, LES reduce the dependency on modelling to the smallest, unresolved scales. Hence, the quest for an universal RANS model representing the whole range of turbulent scales and encompassing all physical situations is given up on profit of models, called subgrid-scale models, accounting for small scales only [1–4]. A particular area which may benefit from LES concerns transitional flows. In such flows, the turbulence, which is not present at the beginning, must be predicted as the result of the multiple instabilities developing from the laminar state. The RANS assumption of well-developed turbulence is no longer legitimate in that case and a non-stochastic approach such as LES can be viewed as a viable alternative.

This paper describes an application of a finite volume (FV)/finite element (FE) numerical method in conjunction with LES models to predict transition in a vortex submitted to compression. The problem considered in the following is related to an internal combustion engines configuration called 'tumble', consisting in a large-scale vortical flow whose axis is perpendicular to the piston velocity. The tumble is usually generated during the intake phase, due to a special arrangement of the inlet port. One advantage of the 'tumble' is that it breaks up at some stage of compression producing a high level of turbulence, beneficial to mixing and combustion. An experimental study of the tumble has recently been carried out in a simplified configuration using a square-piston machine [5, 6]. For this particular flow case, the performance of different RANS models has been also assessed [7], providing rather mixed conclusions. A positive achievement of the RANS method concerns the prediction of the mean tumble velocity during the intake phase, especially when second-order turbulence models are used. Less positive is the fact that all models tested in Reference [7] fail in predicting the very prominent maximum observed in the distribution of turbulent kinetic energy around the centre of the vortex. The large degree of coherence of these velocity fluctuations, which can be explained by a precession effect of the vortex core, is one reason for expecting that LES is more appropriate to this case. In addition, the poor quality of the RANS predictions in the late stage of compression was also an incentive for a detailed analysis of the tumble breakdown.

LES have recently been performed [8] of the tumble experiment [6]. The non trivial nature of the configuration, including both intake and compression phases as in real engine flows, was a motivation for using a numerical method based on unstructured meshes. Connected to this study, different tests on numerics and subgrid models have been carried out including comparisons to direct numerical simulations (DNS) of simpler flows. The purpose of this paper is to report some of these tests, and more specially those related to the Taylor vortex submitted to a compression, which is a simplified situation illustrating some important aspect of the tumble dynamics.

In the context of the numerical flow simulation, using unstructured meshes is often considered as an advantageous means of dealing with complex geometrical features such as those imposed by the flow boundaries or by the necessity of local grid refinements. However, numerical schemes on unstructured meshes are often limited to second order even if those schemes may have higher accuracy on regular grids. LES using second-order accurate schemes with regular and non-regular grids have been successfully applied to a large number of flows [9–12]. Fewer references exist on the application of LES to internal engine flows [8, 13, 14].

The present numerical method is based on a mixed FV/FE discretization of the compressible Navier–Stokes equations. The numerics uses a second-order accurate MUSCL upwind scheme whose spatial dissipation is controlled by a parameter α. A critical point in the application of this method to LES is the control of the numerical dissipation. A minimal amount of numerical dissipation is needed to stabilize the numerical scheme but it is also desirable that the dynamics of the resolved scales remain only marginally affected by this artefact. One purpose of this paper is to analyse the interaction of this numerical dissipation with that introduced by the subgrid scale model.

As a preliminary test, LES results are presented in a case of decaying homogeneous isotropic turbulence. Different subgrid models are compared and the influence of the upwinding parameter is studied. The second test case concerns the compressed Taylor vortex. Two different values of the Reynolds number are considered. The lower Reynolds case is simulated without subgrid model. At the higher value, turbulence transition occurs and the simulation is performed with the use of a subgrid model. For both values, the results are compared to DNS data, obtained by a spectral code. The influence of the upwinding parameter α and its interaction with the effect of the subgrid-scale model are also discussed.

The paper is organized into three parts. Section 2 provides a brief description of the subgrid models. Section 3 concerns the numerical method and the adaptation of LES models to unstructured grids. The results are presented in Section 4, first for homogeneous isotropic turbulence and finally for the compression of the Taylor vortex.

2. GOVERNING EQUATIONS

2.1. *Filtered equations*

The equations used by LES are intended to represent the larger-scale motion of the flow. Distinction between large scales and the whole field is made by applying a low-pass filter on the physical variables and the associated conservation laws. When the filter is homogeneous and thus commutes with differential operators, a relatively simple set of equations can be obtained. Regarding compressible flows, as those considered thereafter, the filtered equations can be expressed as in Reference [15]:

$$\frac{\partial \bar{\rho}}{\partial t} + \frac{\partial \bar{\rho} \widetilde{u}_j}{\partial x_j} = 0 \tag{1}$$

$$\frac{\partial \bar{\rho} \widetilde{u}_i}{\partial t} + \frac{\partial \bar{\rho} \widetilde{u}_i \widetilde{u}_j}{\partial x_j} + \frac{\partial \bar{p}}{\partial x_j} - \frac{\partial \check{\sigma}_{ij}}{\partial x_j} = -\frac{\partial \bar{\rho} \tau_{ij}}{\partial x_j} + R_m \tag{2}$$

$$\frac{\partial \bar{\rho} \check{E}}{\partial t} + \frac{\partial (\bar{\rho} \check{E} + \bar{p}) \tilde{u_j}}{\partial x_j} - \frac{\partial \check{\sigma}_{ij} \tilde{u_i}}{\partial x_j} + \frac{\partial \check{q}_i}{\partial x_i} = \tilde{u_i} \frac{\partial \bar{\rho} \tau_{ij}}{\partial x_j} + R_E \tag{3}$$

The filtered quantities are marked with overlines and the Favre-filtered ones (density weighted) with tildes (e.g. $\tilde{u} = \overline{\rho u} / \bar{\rho}$). This set of equations is complemented by the equation of state. For perfect gases:

$$\bar{p} = r \bar{\rho} \widetilde{T} \tag{4}$$

The left-hand sides of Equations (1)–(3) are directly computable either from 'resolved' quantities like velocity $\widetilde{u}_i$, temperature $\widetilde{T}$, density $\bar{\rho}$, pressure $\bar{p}$, or from the 'computable' quantities

$\check{E}$, $\check{\sigma}_{ij}$ and $\check{q}_i$ used in place of the filtered expressions for total energy, viscous stress and heat flux:

$$\check{E} = \frac{1}{\gamma - 1}\,\frac{\bar{p}}{\bar{\rho}} + \frac{1}{2}\widetilde{u}_i\widetilde{u}_i \tag{5}$$

$$\check{\sigma}_{ij} = \mu(\widetilde{T})\left(\frac{\partial \widetilde{u}_i}{\partial x_j} + \frac{\partial \widetilde{u}_j}{\partial x_i} - \frac{2}{3}\frac{\partial \widetilde{u}_k}{\partial x_k}\delta_{ij}\right) \tag{6}$$

$$\check{q}_i = -\lambda(\widetilde{T})\frac{\partial \widetilde{T}}{\partial x_i} \tag{7}$$

The subgrid terms have been placed in the right-hand sides of Equations (1)–(3), representing expressions that are not directly computable from the resolved quantities and requiring a specific closure. Among all these terms, the most important are the terms involving the subgrid stress tensor:

$$\tau_{ij} = \widetilde{u_i u_j} - \widetilde{u}_i\widetilde{u}_j \tag{8}$$

The remaining terms R_m and R_E are neglected in the following as it is usual to do for the low Mach number and nearly isothermal flows considered in this study.

2.2. Smagorinsky model

The Smagorinsky model [16] relates the deviatoric part of the subgrid tensor to the filtered velocity gradient by a linear eddy-viscosity model:

$$\tau_{ij} - \tfrac{1}{3}\tau_{kk}\delta_{ij} = -2C_{\mathrm{s}}^2\Delta^2|\overline{S^{\mathrm{d}}}|\overline{S^{\mathrm{d}}_{ij}} \tag{9}$$

$$\overline{S^{\mathrm{d}}_{ij}} = \frac{1}{2}\left(\frac{\partial \tilde{u_i}}{\partial x_j} + \frac{\partial \tilde{u_j}}{\partial x_i}\right) - \frac{1}{3}\delta_{ij}\frac{\partial \tilde{u_k}}{\partial x_k} \tag{10}$$

where Δ denotes the filter width and $|\overline{S}|$ the characteristic filtered rate of strain:

$$|\overline{S}| = (2\overline{S^{\mathrm{d}}_{pq}}\,\overline{S^{\mathrm{d}}_{pq}})^{1/2} \tag{11}$$

For low Mach number flows considered thereafter, τ_{kk} is negligible as compared to the thermodynamic pressure and thus ignored [17]. In the following, the classical value $C_{\mathrm{s}} = 0.17$ is used. This choice, originated with the analysis of Lilly and presented of the book of Pope [2], is usually considered as satisfactory for isotropic turbulence near spectral equilibrium.

2.3. Dynamic Smagorinsky model

The major criticism against the Smagorinky model is that the value C_{s} is not universal. In particular, it has been clearly attested that the value $C_{\mathrm{s}} = 0.17$ must be attenuated near solid walls and in transitional flows. To compensate for these variations, a modification of the Smagorinsky model has been proposed by Germano *et al.* [18]. The constant C_{s}^2 in Equation (9) is replaced by a coefficient C_{d} depending on the local structure of the flow.

In order to compute C_d, a filter test is introduced whose width $\widehat{\Delta}$ is larger than Δ. Application of this filter to a variable x is denoted by $\hat{x}$. The coefficient C_d is calculated with a least squares approach according to:

$$C_\mathrm{d} = \frac{M_{ij}L_{ij}}{M_{ij}M_{ij}} \tag{12}$$

$$L_{ij} = \widehat{\overline{u_i u_j}} - \hat{\overline{u}}_i \hat{\overline{u}}_j \tag{13}$$

$$M_{ij} = -2\widehat{\Delta}^2 |\widehat{\overline{S^\mathrm{d}}}| \widehat{\overline{S^\mathrm{d}_{ij}}} + 2\Delta^2 \widehat{|\overline{S^\mathrm{d}}| \overline{S^\mathrm{d}_{ij}}} \tag{14}$$

In the dynamic model, the occurrence of negative values of C_d is a factor of numerical instability. For flows having directions of statistical homogeneity, this problem is usually remedied by taking the averaged values of the numerator and the denominator in Equation (12). No such possibility exists in the Taylor vortex problem and a local smoothing is applied to avoid unphysical oscillations of C_d. This coefficient will also be set to zero when the sum of the subgrid and the molecular dissipation is negative.

3. NUMERICAL METHOD

3.1. Basic numerical method

The filtered equations are written in the symbolic form:

$$\frac{\partial W_i}{\partial t} + \mathrm{div}(F(W)) = \mathrm{div}(R(W)) + S(W) \tag{15}$$

where $W = [\rho, \rho u_1, \rho u_2, \rho u_3, \rho E]$ represents the vector of the conservative variables, $F(W)$ the convective fluxes of W, $R(W)$ the diffusive fluxes and $S(W)$ the source terms. The numerical method is based on a mixed FV/FE discretization [19].

For the hyperbolic part of the equations a FV approximation is used together with a Riemann solver. Diffusive and source terms are discretized using a Galerkin method with a P1 FE interpolation. The method is implemented using 3D unstructured meshes in a numerical code ('NadiaLES') dedicated to LES in complex geometry [20]. Several examples (temporal mixing layers, flow around a square cylinder, combustion chamber) are described in Reference [20].

The numerical method uses unstructured tetrahedrizations of the computational domain Ω and is a vertex-centred scheme (i.e. all degrees of freedom are located at vertices). A dual FV mesh is built by the rule of medians (see Figure 1 for a 2D grid). A cell C_i is constructed around each vertex (i) by joining the centres of two neighbouring tetrahedrons with the middle of their common side. On this grid, the weak formulation of Equation (15) reads:

$$\int_\Omega \left(\frac{\partial W_i}{\partial t} + \mathrm{div}(F(W)) \right) \psi_i \, \mathrm{d}v = -\int_\Omega \mathrm{div}(R(W)) N_i \, \mathrm{d}v + \int_\Omega S(W) N_i \, \mathrm{d}v \tag{16}$$

where the test functions are the FE basis functions N_i for the diffusion and source terms and the characteristic functions ψ_i of the cell C_i for the Euler terms (convection and pressure terms).

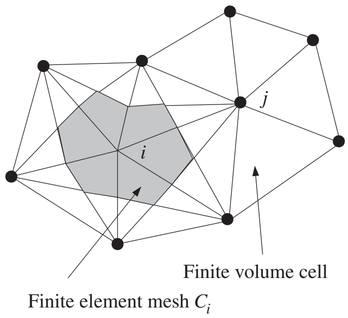

Figure 1. 2D finite element mesh and finite volume cell.

After integration by part, this mixed variational formulation becomes:

$$\int_{C_i} \frac{\partial W_i}{\partial t}\,\mathrm{d}v + \int_{\partial C_i} F(W)\,\mathrm{d}s = -\int_{\Omega} R(W).\nabla(N_i)\,\mathrm{d}v + \int_{\Omega} S(W)N_i\,\mathrm{d}v \tag{17}$$

The discretization of the convective fluxes $F(W)$ on the cell boundaries is obtained by a Roe flux difference splitting technique [21], which is an upwind-biased scheme along the characteristic lines. Convective fluxes through the boundary ∂C_i are the sum of the fluxes through the common boundary between two adjacent cells:

$$\int_{\partial C_i} F(W).n\,\mathrm{d}\Gamma = \sum_{j\in K(i)} \int_{C_{ij}} F(W).n\,\mathrm{d}\Gamma \tag{18}$$

where $K(i)$ is the set of neighbouring nodes for the vertex i. The flux between two adjoining cells C_i and C_j, denoted Φ_{ij}, can be written as a sum of a centred approximation and an additional dissipation term (the upwind term), whose effect is of stabilizing the centred scheme:

$$\Phi_{ij} = \Phi(W_i, W_j, n_{ij}) = \left(\frac{F(W_i, n_{ij}) + F(W_j, n_{ij})}{2}\right) - \frac{1}{2}d(W_i, W_j, n_{ij}) \tag{19}$$

In this expression, n_{ij} denotes the normal at the cell boundary and W_i and W_j the quantities W evaluated at the centre of the cells.

For the Roe scheme the fluxes are evaluated as

$$\Phi_{ij} = \Phi(W_i, W_j, n_{ij}) = \underbrace{\left(\frac{F(W_i, n_{ij}) + F(W_j, n_{ij})}{2}\right)}_{\text{centred part}} - \frac{1}{2}\underbrace{|A(\tilde{W}, n_{ij})|(W_j - W_i)}_{\text{upwind part}} \tag{20}$$

in which $A = \partial F/\partial W$ is the Jacobian matrix of the fluxes $F(W)$ and $\tilde{W}$ the Roe's average of W_i and W_j.

The spatial accuracy of this scheme is only of first order and a second-order scheme is obtained with the MUSCL linear reconstruction method introduced by Van Leer [22]. The idea consists in replacing W_i and W_j by the interpolated values W_{ij} and W_{ji} on the interface between the two cells centred at the nodes i and j.

$$W_{ij} = W_i + \tfrac{1}{2}(\nabla W)_i^D.\boldsymbol{ij} \tag{21}$$

$$W_{ji} = W_j - \tfrac{1}{2}(\nabla W)_j^D.\boldsymbol{ij} \tag{22}$$

$(\nabla W)_i^D$ is an approximate gradient of W at each vertex, derived from the Galerkin linear interpolation of W over all the neighbouring triangles (see Reference [11])

$$(\nabla W)_i = \frac{1}{\text{meas}\, C_i} \sum_{T, i \in T} \int_{C_i \cap T} \nabla W_h \, \mathrm{d}w \tag{23}$$

The time integration is performed using an explicit fourth-order Runge–Kutta method. An efficient parallel implementation has been done using a domain decomposition method and the message-passing libraries.

3.2. Adaptation of the numerical method to LES

The main criticism against using upwind second-order schemes for LES is their excessive numerical dissipation, which can override the dissipation due to the subgrid-scale model. To control certain properties of the discretization, the standard formulation has been modified by introducing two adjustable parameters, α and κ.

The parameter 0.5, in front of the upwind part of the Roe fluxes in Equation (20), is replaced by a coefficient α giving the possibility to adjust the numerical viscosity to the smallest value, compatible with the stability of the numerical scheme [23]:

$$\Phi_{ij} = \frac{F(W_{ij}) + F(W_{ji})}{2} - \alpha |A(\tilde{W}, n_{ij})|(W_{ji} - W_{ij}) \tag{24}$$

A minimal amount of numerical spatial dissipation is mandatory since this dissipation directly competes with the effect of the second derivatives of the subgrid-scale model. But a too low amount of dissipation induces non-physical oscillations in the solution, which then becomes numerically unstable (the case $\alpha = 0$ is unconditionally unstable). The parameter α is then chosen, in each test case, as the smallest value for which non-physical oscillations are avoided.

The second parameter κ controls the dispersion rate of the interpolation. The interpolation of W_i and W_j on the interface is evaluated through a balance between a centred gradient $(\nabla W)^C$ and an approximate gradient on the vertex $(\nabla W)^D$.

$$W_{ij} = W_i + 0.5[(1 - 2\kappa)(\nabla W)^C + 2\kappa(\nabla W)_i^D].\boldsymbol{ij} \tag{25}$$

$$W_{ji} = W_j - 0.5[(1 - 2\kappa)(\nabla W)^C + 2\kappa(\nabla W)_j^D].\boldsymbol{ij} \tag{26}$$

The term $(\nabla W)^C.\boldsymbol{ij}$ is defined as

$$(\nabla W)^C.\boldsymbol{ij} = W_j - W_i \tag{27}$$

For $\kappa = \frac{1}{3}$, the interpolation is third-order accurate for the 1D advection problem on regular mesh problem [11].

The Roe solver is known to suffer from accuracy problems in the low Mach number limit [24]. To extend the numerical method to low velocity flows, a preconditioning technique is commonly used. In this study, the preconditioning method of Guillard is employed [24–26].

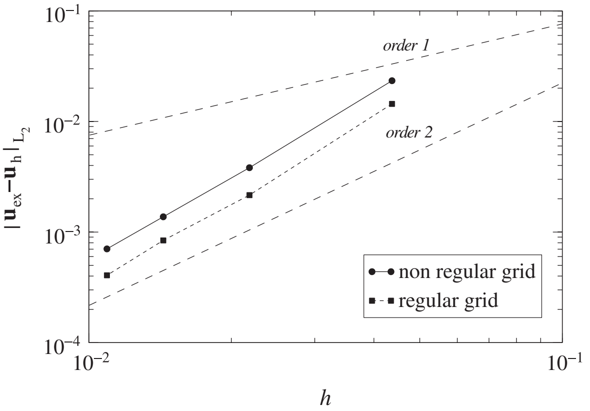

Figure 2. L_2 norm of the difference between exact velocity $\mathbf{u}_{ex}$ and approximate solution $\mathbf{u}_h$ as function of the mesh size h.

The Roe matrix $|A(\tilde{W}, n_{ij})|$ in the upwind part of the fluxes is replaced by $P_c^{-1}|P_c A(\tilde{W}, n_{ij})|$ where P_c is a preconditioning matrix, which can be written in primitive variables as $P_p = \text{Diag}(\beta^2, 1, 1, 1, 1)$ in which β is a parameter of the order of the Mach number of the flow.

The overall accuracy of the numerical method is demonstrated by comparing the results obtained on 2D regular and non regular grids to the analytical solution of the Taylor vortex flow. The computational domain is a square and shear-free conditions are applied to the boundary. The flow is first calculated on different regular grids and the L_2 norm of the error is evaluated as function of the mesh size h. In order to ascertain the sensitivity to the non-regular character of the unstructured meshing, the simulation is also performed after applying large random displacements to the nodes of the different regular grids. The grid modification is such that the probability law of a node displacement from its initial position is uniform within a radius equal to 75% of the original mean mesh size. The results are plotted in Figure 2 and show a second-order accuracy for both sets of grids.

The Taylor vortex considered in this paper is a case of flow evolving inside a parallepipedic domain whose edge length in the x_1 direction is a decreasing function of time $a(t)$. To take into account the domain deformation, a simple moving mesh formulation is employed. The domain is turned into a fixed one by the coordinate transformation $X_1 = x_1\, a(0)/a(t)$, $X_2 = x_2$, $X_3 = x_3$, where $a(0)$ is the side-length at initial time. The equations are solved in the new system of coordinates on a unique mesh, corresponding to the geometry at initial time.

3.3. *Adaptation of the filtering to non-structured grids*

As usual, it is considered that the 'resolved' scales are filtered by the effect of the numerical discretization. No explicit filter is used, except for the test filter of the dynamic Smagorinsky model. For non-regular grids, the filter parameter Δ depends locally on the mesh size. At vertex (i), Δ is defined as the characteristic size of the corresponding cell C_i:

$$\Delta = \text{meas}(C_i)^{1/3} \tag{28}$$

The size of the test filter attached to the vertex (i), is the size of the super-cell resulting from the union $K(i)$ of all the neighbouring cells C_j:

$$\widehat{\Delta} = \left(\sum_{K(i)} \text{meas}(C_j) \right)^{1/3} \tag{29}$$

One problem in estimating C_d locally from Equation (12) is that the obtained values have frequently strong variations in space with potentially negative impact on the stability of the LES calculations. When feasible, the constant C_d is averaged in directions of statistical homogeneity. In the present case, no such possibility exists and the nodal value C_d is simply taken as the volume average of the dynamic constant on all the neighbouring nodes.

4. LES RESULTS

4.1. Decay of homogeneous isotropic turbulence

The numerical method is first applied to the LES of homogeneous isotropic turbulence. Widely documented by experimental data or DNS, this configuration is a standard test for the LES methods. In the absence of mean velocity gradient or external forces, the kinetic energy of the flow decays due to effect of viscosity. A too strongly dissipative method is usually diagnosticed by an increase of the energy decay rate and a loss of resolution in the small-scale range. Here, the influence of the subgrid model and the role of the mesh and of the upwinding parameter α on the numerical dissipation are investigated.

For the present LES, the reference data are from the grid-generated turbulent flow of Comte-Bellot and Corrsin [27]. In a frame moving with the mean velocity, this flow is viewed as a freely decaying, homogeneous, isotropic turbulence and simulated in a cubic box with periodic boundary conditions in the three directions. Energy spectra have been measured at three downstream locations from the grid corresponding to the dimensionless times: $U_0t/M = 42$, 98, 171, in terms of grid mesh size unit $M = 5.08\,\text{cm}$ and mean velocity at the grid section $U_0 = 10\,\text{m/s}$.

The simulations are performed with a 32^3 nodes grid in a numerical box whose sides are 32 cm long. The initial divergence-free velocity field is generated in Fourier space in a conventional manner. Its energy spectrum matches the experimental data at $U_0t/M = 42$.

The results corresponding to the two subgrid-scale models are first compared for the value $\alpha = 0.025$. Note that for this low value of α, numerical instabilities are obtained if the subgrid-scale model is removed from the equations. Direct simulation is possible however when the value of the parameter is raised to $\alpha = 0.1$. Time evolutions of kinetic energy are shown in Figure 3 while the energy spectra $E(K)$ are plotted in Figure 4 for the initial state at $U_0t/M = 42$ and for 98. Obviously, the contribution of the subgrid scales is not included in the LES results. If the effect of the discretization is approximated by the effect of a top-hat filter at the mesh spacing, this contribution is estimated at about 10% of the total kinetic energy. The corrected experimental data are also plotted in Figure 3. The figures also show that the dynamic Smagorinsky model is slightly less diffusive than the standard Smagorinsky model but the difference between the models is very weak. The results of the coarse DNS

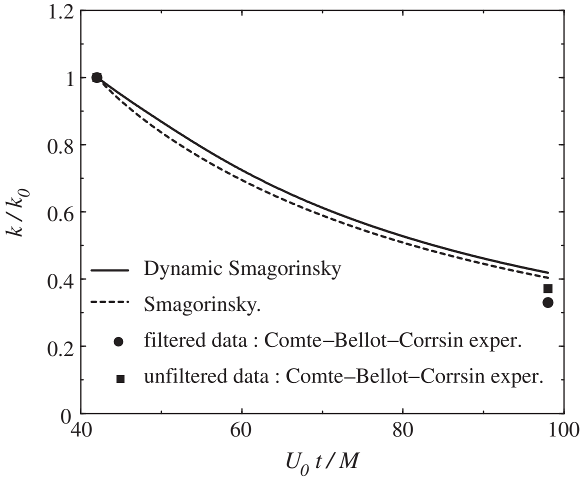

Figure 3. Decay of turbulence kinetic energy. Influence of the subgrid model. Comparison to Comte-Bellot and Corrsin experiment [27].

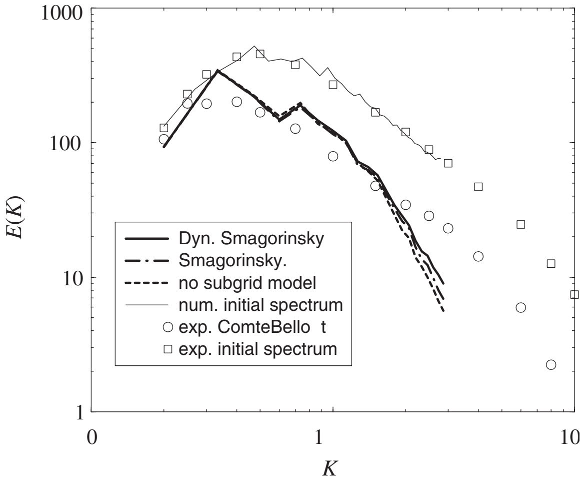

Figure 4. Energy spectrum at initial time and at the non-dimensional time $U_0t/M = 98$. Influence of the subgrid model. Comparison to Comte-Bellot and Corrsin experiment [27].

(no subgrid model) have also be plotted in Figure 4. Very likely, the slightly more diffusive character of the coarse DNS can be explained by the larger value of α.

Considering now the effect of the upwinding parameter α, Figures 5 and 6 present the kinetic energy and the spectra for the three values $\alpha = 0.025$, 0.05 and 0.1. All curves are relative to the dynamic Smagorinsky model. It is clearly apparent that too much upwinding increases the energy decay rate. The diffusive character of high values of α is also attested in Figure 6 for the high wavenumber range. It follows that the parameter α must then be

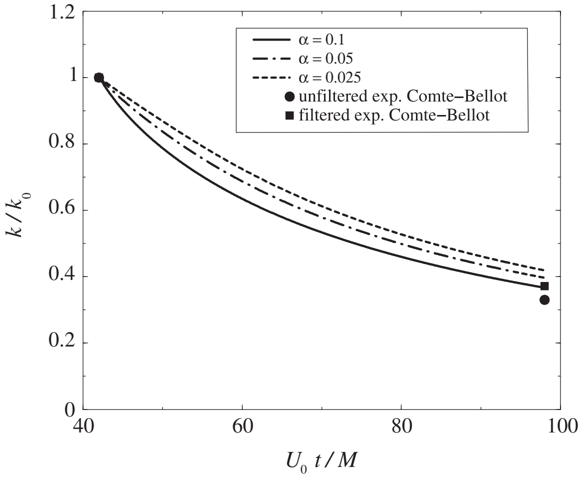

Figure 5. Decay of turbulence kinetic energy. Influence of the numerical viscosity parameter α.

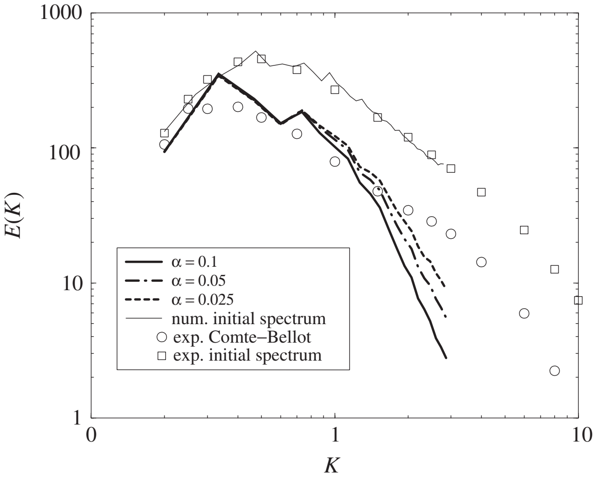

Figure 6. Energy spectrum at initial time and at $U_0t/M = 98$. Influence of the numerical viscosity parameter α.

reduced as far as possible in order to obtain reliable results. A minimal value of α is however mandatory to prevent numerical instabilities and the value 0.025 appears in this case not to be far from the optimum.

Additional tests have been performed to analyse the influence of the grid regularity. A simulation is performed on a non-uniform 32^3 nodes grid whose the mesh aspect ratio varies from 1 (at the centre) to 3 (near the domain limits). Another non-regular 32^3 grid has been considered, obtained from a random perturbation of the nodes of a uniform square mesh, as described in Section 3.3. Results for the spectra are compared in Figure 7. The random

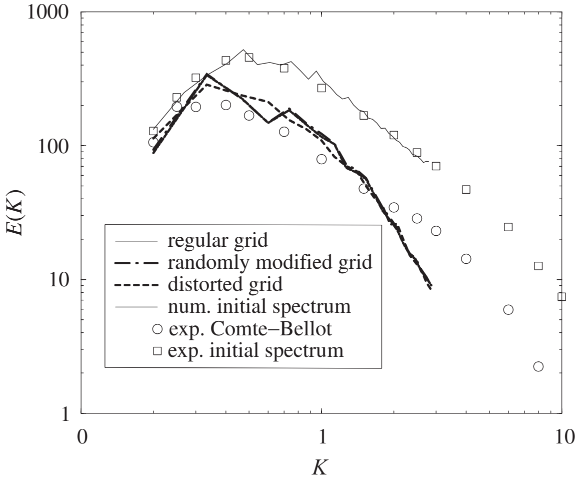

Figure 7. Energy spectrum at initial time and at $U_0t/M = 98$. Influence of the grid regularity.

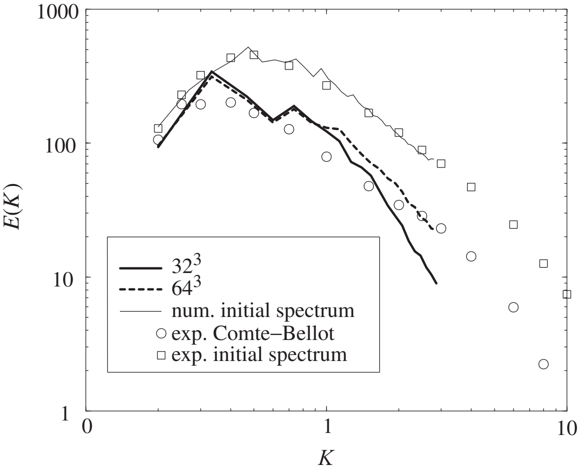

Figure 8. Energy spectrum at initial time and at $U_0t/M = 98$. Influence of mesh refinement.

perturbations of the nodes do not change the results compared to the regular mesh. For the non-regular mesh, the results are only slightly modified in the large scales. A simulation has also been performed on a refined mesh (64^3). The only visible effect is a better resolution in the small scales (Figure 8).

As expected, the numerical diffusivity and the rate of kinetic energy drained by the subgrid model increase with the upwinding parameter. The effects of the subgrid-scale viscosity and numerical viscosity are however far from being additive. To illustrate how they are interlinked which each other, the quantities C_d and μ_t/μ for the dynamic model have been plotted for the three values of α. The time evolutions presented in Figures 9 and 10 are obtained by averaging

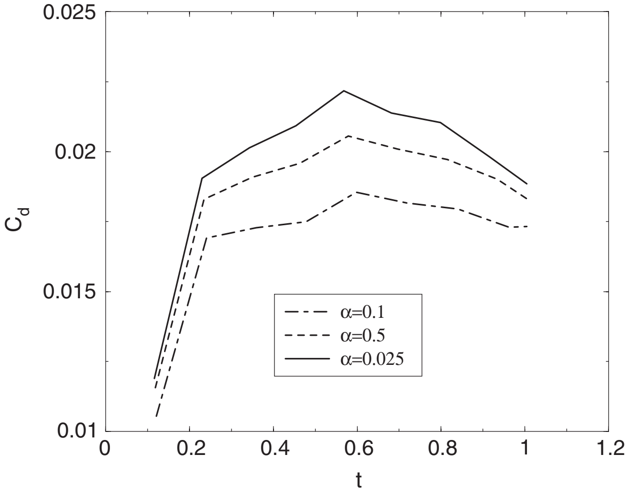

Figure 9. Time evolution of the dynamic constant for different values of the upwinding parameter α.

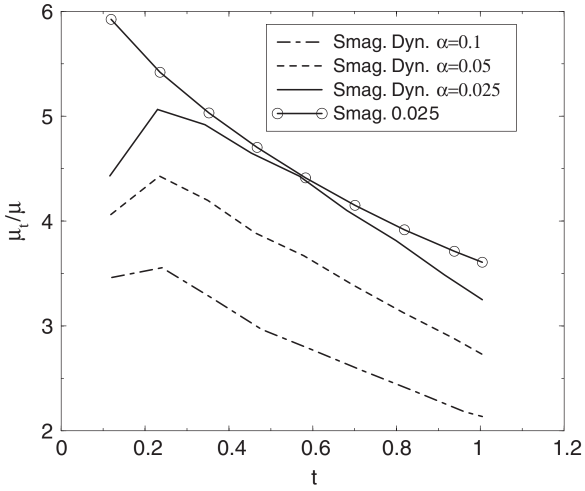

Figure 10. Time evolution of the non-dimensional subgrid viscosity μ_t/μ.

over the whole domain. The subgrid-scale viscosity obtained by the standard Smagorinsky model is also plotted for $\alpha = 0.025$.

After a short transition period, C_d saturates to a nearly constant value that appears to be a decreasing function of α. The different values of C_d remain smaller than the Smagorinsky model coefficient $C_s^2 = 0.0289$. The subgrid viscosity has typical decreasing variations due to the decay of turbulent energy and, for the considered time lap, μ_t is three to five times larger than the molecular viscosity. As noted before, for equal values of $\alpha = 0.025$, the dynamic model is slightly less diffusive than the standard model. Like the coefficient C_d, μ_t/μ

decreases when α increases. To a certain extent, this variation results from the linear relation between the two parameters. But, while the relative variations of C_d lie between 10 and 20%, those of μ_t/μ go up to 40–50%. The fact that C_d is lower when the numerical method is more diffusive can be explained by the decrease of residual stress, relative to the test filter. The larger decrease of μ_t/μ results from the reduction of the filtered strain rate when larger values of α are used.

4.2. Compression of the Taylor vortex

The investigation is now turned to the case of the Taylor vortex flow submitted to a compression in a direction perpendicular to the vorticity vector. This flow is of particular relevance in the context of internal combustion engines. One particular reason is the existence of an analytical solution for the 2D Taylor vortex problem to which numerical simulations can be directly compared. A property of the Taylor vortex that makes it viewed as a possible model for the tumble breakdown, is the possibility for 3D instabilities to develop, when the vortex is submitted to deformation. When the Reynolds number is high enough, a turbulent flow emerge from these instabilities, making this flow also relevant for subgrid-scale models assessment. In the last instance, due to its particular boundary conditions, the Taylor vortex can be simulated using Fourier-type spectral expansions. These methods have fast convergence properties and are easy to implement. DNS in the turbulent regime can thus be carried out at reasonable computational cost in order to provide reference data for the LES predictions. The characteristics of the Taylor vortex test cases are now exposed, followed by a short account of the spectral method used to obtain the reference data. The numerical results of the FE–FV method are then presented, including DNS and LES cases and comparisons to data from the spectral method.

4.2.1. Description of the test case. Consider the time-varying, parallelepipedic domain: $0<x_1<a(t)$, $0<x_2<a_0$, $0<x_3<a_0$, submitted to a deformation in the x_1 direction. At time $t=0$, the domain is supposed to be cubic: $a(0)=a_0$ and the fluid flow inside is defined by the velocity $\mathbf{u}=\nabla\times\psi\mathbf{x}_3$ and the streamfunction

$$\psi=\frac{a_0^2\Omega_0}{2\pi^2}\sin\frac{\pi x_1}{a_0}\sin\frac{\pi x_2}{a_0} \tag{30}$$

This expression corresponds to the well-known Taylor–Green vortex solution. In infinite space, the velocity field consists in a periodic arrangement of counter-rotating vortices decaying with the exponential factor $\exp(-2\nu\pi^2 a_0^{-2}t)$. The restriction to the cubic domain defines one unique vortex tangent to the cube and referred to hereafter as the 'Taylor vortex'. By virtue of the flow symmetries, this vortex considered from its own part can be viewed as a solution in the cube with 'shear-free' boundary conditions, consisting in zero mass flux and zero tangential shear conditions.

In the same way, a two-dimensional analytical solution can be obtained for the above-considered time-varying domain and the same type of boundary conditions. The solution of Le Roy and Le Penven [7] represents the Taylor vortex submitted to compression (or dilatation) in the direction x_1 perpendicular to the initial vorticity. This solution, the so-called 'compressed Taylor vortex', is obtained assuming that: (i) the flow Mach number is very small, (ii) the boundaries are thermally isolated, (iii) the density has uniform values at initial time. Under these assumptions, the density remains spatially homogeneous and varies in time as the compression ratio $r(t)=a(t)/a(0)$.

For a time-independent domain having unequal sidelengths in x_1 and x_2 directions, a solution also exists generalizing Equation (30). While the Taylor vortex is linearly stable when the sidelengths in the two directions are equal, instability is proved in the general case if the Reynolds number is large enough [28, 29]. In the same spirit, it has been shown that the compressed Taylor vortex can produce a very complex, three-dimensional flow under the effect of a small initial perturbation [7]. The following case is such an example of initially perturbed Taylor vortex undergoing compression.

The perturbation introduced at $t=0$ consists in a secondary Taylor vortex perpendicular to the first one and rotating in the x_1, x_3 plane. The perturbation velocity reads $\nabla \times \psi' \mathbf{x}_2$, where

$$\psi' = \varepsilon \frac{a_0^2 \Omega_0}{2\pi^2} \sin \frac{\pi x_1}{a_0} \sin \frac{\pi x_3}{a_0} \tag{31}$$

The perturbation amplitude is fixed to 1% of the velocity of the main vortex ($\varepsilon = 0.01$). Introducing the Reynolds number $Re = \Omega_0 a_0^2/v$ based on Ω_0, the maximum value of the initial vorticity, three different values are considered: $Re = 1600$, 6250, 78 300. For each case, the kinematic viscosity v is maintained constant. The boundary conditions are of shear-free type. The variable side-length $a(t)$ is specified by the decreasing function:

$$a(t) = a_0 + \frac{V_0}{\omega}[1 - \cos(\omega t)] \tag{32}$$

for time t varying from 0 to π/ω. The compression depends on two parameters, the maximum value of the volumetric ratio: $r(\pi/\omega)=5$ and the ratio of the time scales corresponding to the vortex and to the compression which is equal to $\Omega_0/\omega = 20.4$. These values have been chosen in reference to the tumble experiment described in Reference [5]. For the first two values of Re, the flow remains laminar and is simulated directly, without turbulence modelling. For the higher Reynolds number value, the flow becomes turbulent during the compression phase and the subgrid-scale model is activated. All the simulations are performed assuming that initial density is spatially uniform and the domain boundaries are thermally isolated. The initial Mach number M is fixed to a small value, in order that the $O(M^2)$ inhomogeneities of density, temperature and velocity divergence remain negligible.

Reference data are obtained by using a spectral code based on a Fourier pseudo-spectral method. The compression-induced velocity (whose divergence is uniform in space) is removed from the flow velocity and the resulting vector field $\mathbf{u} - \dot{a}/a\, x_1\, \mathbf{x}_1$ is projected on a set of time-varying, complex exponential functions: $\exp(i\pi(h_1 x_1 a_0/a(t) + h_2 x_2 + h_3 x_3)/a_0)$, where h_1, h_2, h_3 are integers. This vector field is supposed to be divergence free, in accordance with the hypothesis of low Mach number. The time-evolution of Fourier coefficients are computed using the classical Runge–Kutta fourth-order method [30].

4.2.2. Direct simulation of the compressed Taylor vortex at $Re = 1600$, 6250. The first two cases corresponding to $Re = 1600$, 6250 have been simulated without subgrid modelling. A first idea about the effect of the perturbation is indicated by the isovorticity surfaces $|\nabla \times \mathbf{u}| = C$. Different values of the compression ratio have been chosen and the value of C at each time is taken as half the maximum value of $|\nabla \times \mathbf{u}|$. At $t=0$, the isosurface is aligned with the z-axis and the perturbation is not discernible. For $Re = 1600$ (Figure 11), the perturbation is rapidly

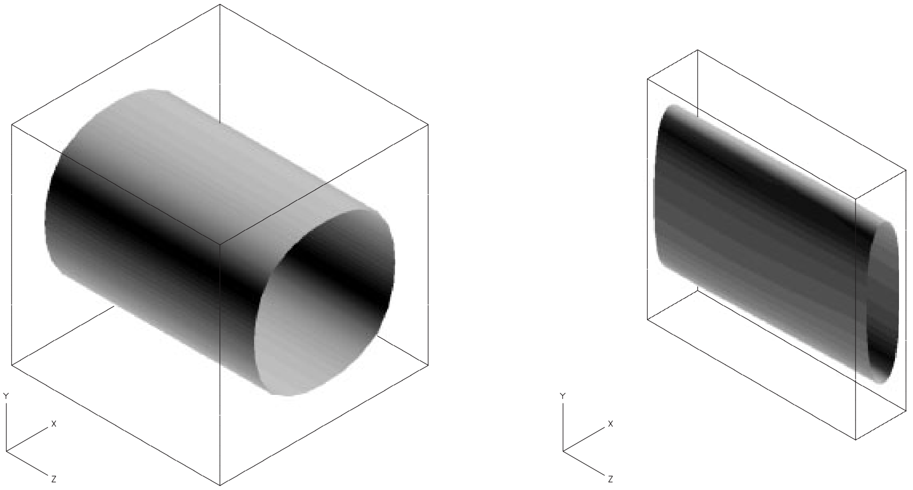

Figure 11. Isosurfaces of vorticity magnitude. $Re = 1600$, $r = 1$ (left) and $r = 5$ (right).

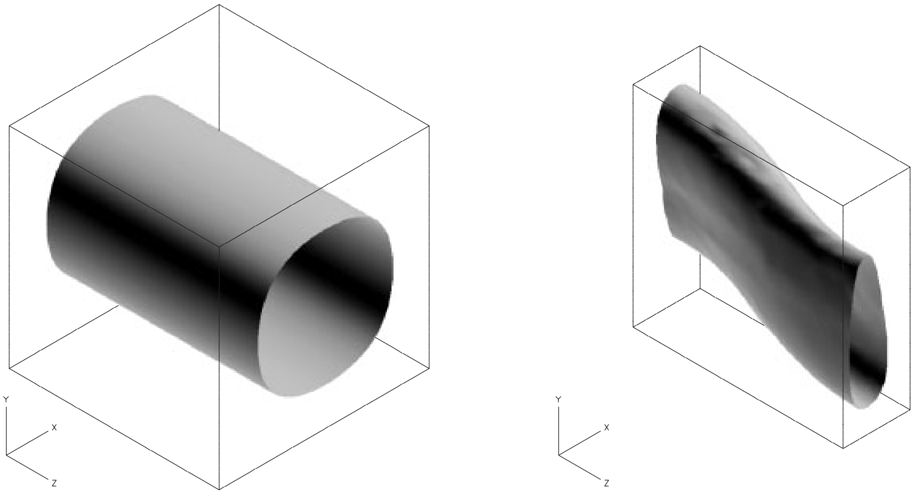

Figure 12. Isosurfaces of vorticity magnitude. $Re = 6250$, $r = 1$ (left) and $r = 3$ (right).

attenuated by the effect of viscosity and the velocity remains very close from Le Roy and Le Penven's [7] two-dimensional solution. On the other hand, the perturbation is clearly amplified in the case $Re = 6250$ and the vortex exhibits a three-dimensional and quite complex behaviour (Figures 12 and 13). The concentration of the isovorticity surface and the emergence of vortex sheets perpendicular to the x_1 direction in Figure 13 are typically non-linear effects. In the last two pictures, one can observe the vortex core, initially oriented in the positive x_3 direction, tilting back in the opposite direction as a consequence of the image ef-

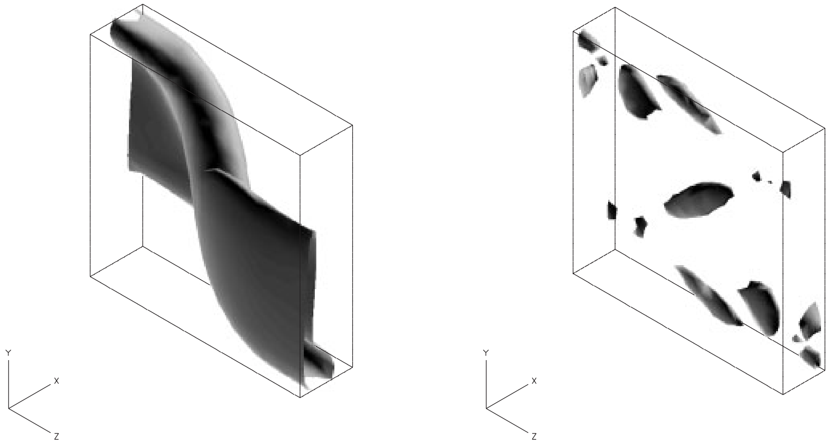

Figure 13. Isosurfaces of vorticity magnitude. $Re = 6250$, $r = 4$ (left) and $r = 5$ (right).

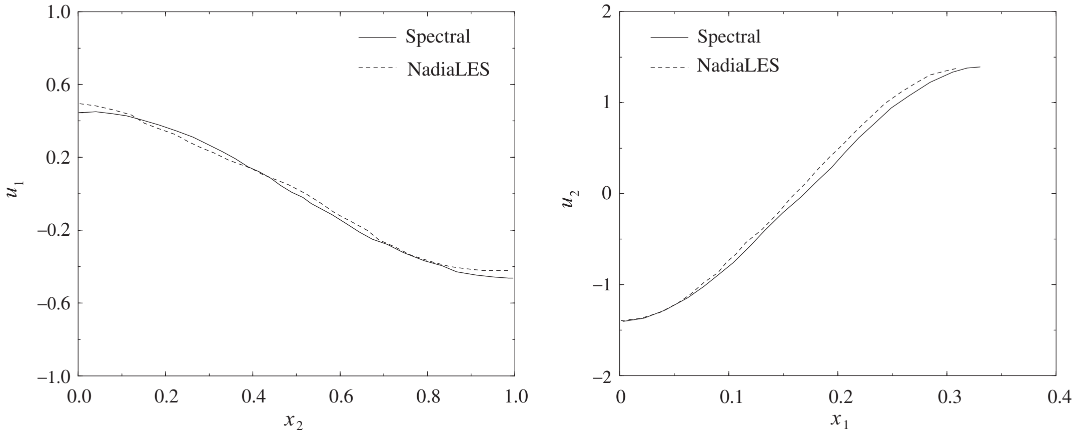

Figure 14. Profiles of $u_1(a/2, x_2, a_0/2)$ and $u_2(x_1, a_0/2, a_0/2)$. $Re = 6250$, $r = 3$.

fect imposed by the boundaries. The simulations have been performed with the FV–FE code using a 81^3 nodes mesh. The results are in good agreement with those obtained by the spectral method, as indicated by the velocity profiles at different stages of compression (Figures 14–16). Note that the compression-induced velocity has been removed from the plotted profiles of u_1.

4.2.3. LES of the compressed Taylor vortex at $Re = 78\,300$. Higher values of the Reynolds number cause a faster increase of the perturbation and, ultimately, the development of a turbulent flow. LES have been performed at $Re = 78\,300$, using the FV–FE method with a 41^3 nodes mesh, different subgrid-scale models and different values of α. The reference data for this LES are produced by a DNS (no subgrid model) using the spectral method. This

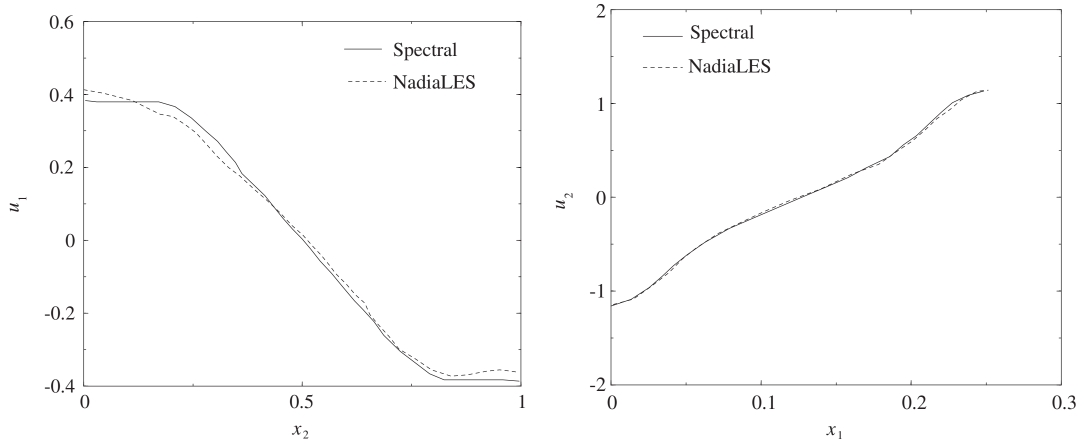

Figure 15. Profiles of $u_1(a/2, x_2, a_0/2)$ and $u_2(x_1, a_0/2, a_0/2)$. $Re = 6250$, $r = 4$.

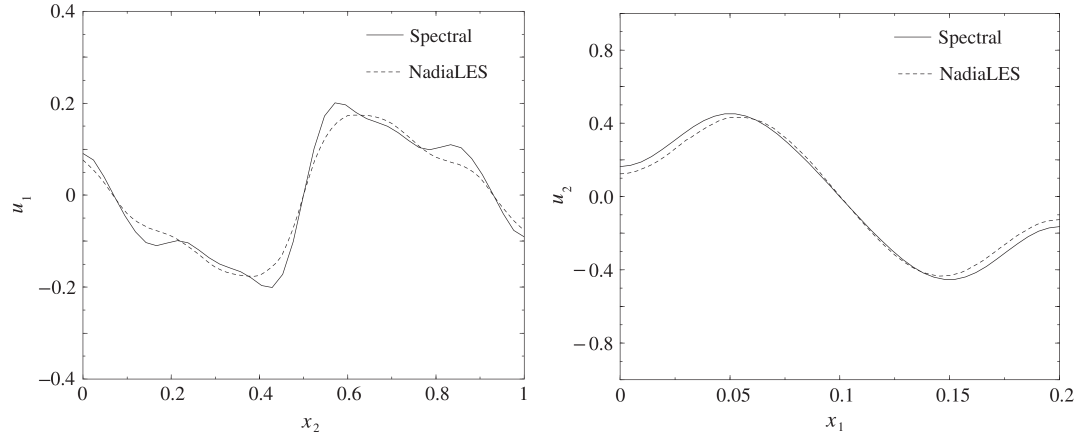

Figure 16. Profiles of $u_1(a/2, x_2, a_0/2)$ and $u_2(x_1, a_0/2, a_0/2)$. $Re = 6250$, $r = 5$.

simulation requires 96×256^2 modes for the second half-part of the compression, when the turbulent transition occurs.

A description of the flow is now given based on the LES results obtained using the dynamic Smagorinsky model and the value $\alpha = 0.025$. From all tested conditions, these ones have been found to be optimal ones as in the case of isotropic turbulent flow of Section 4.1.

Isovorticity surfaces are plotted in Figures 17 and 18 for r equal to 2, 3, 4 and 5. For $r = 2$ and 3, the selected surface corresponds to half its maximum value throughout the flow. The more rapid growth of the instability is apparent when compared to the case $Re = 6250$. At the end of compression, the isovorticity surface exhibits strong irregularities due to the presence of turbulence. For the last two values the isosurfaces correspond to one-quarter of the maximal

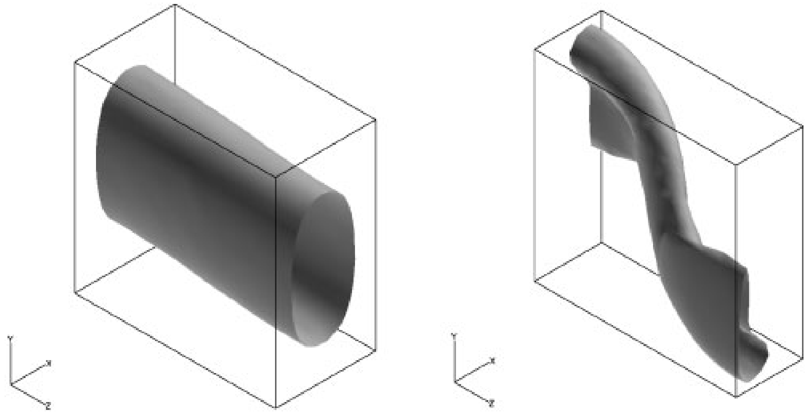

Figure 17. Isosurfaces of vorticity magnitude. $Re = 78\,300$, $r = 2$ (left) and $r = 3$ (right).

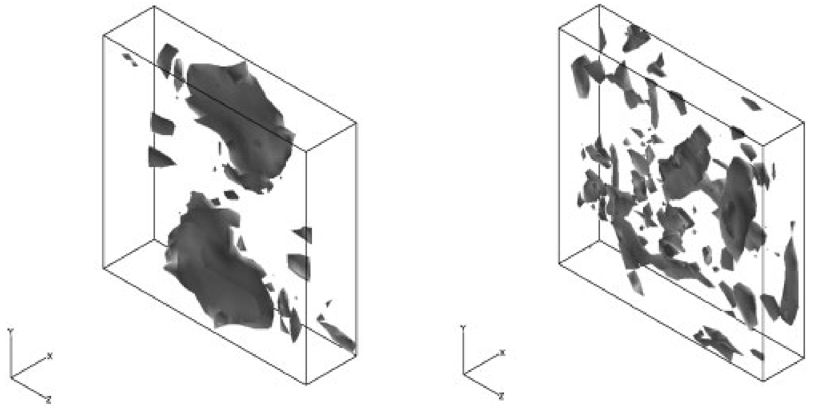

Figure 18. Isosurfaces of vorticity magnitude. $Re = 78\,300$, $r = 4$ (left) and $r = 5$ (right).

value. Transition to turbulence is characterized by an increase of kinetic energy transfer to the smaller scales and is attested around $r = 4$ from the observation of a qualititative change in the spectra of the DNS data. As an illustration, the kinetic energy spectra have been plotted in Figure 19, for the two values $r = 3.02$ and 4.62 and as functions of the three components of wave-vector $K_i = \pi h_i/a_0$. While still rapidly decreasing at $r = 3.02$, the spectra develop almost one decade of inertial range with the characteristic $-5/3$ power law in the last part of the compression. At $r = 4.62$, the three spectra merge in the high wavenumber range, attesting local isotropy in the small scales.

Since the flow is turbulent at the end of compression and becomes very sensitive to small perturbations, arising either from the physics or the numerical approximation, comparing instantaneous profiles for DNS and LES is no longer significant. The analysis will thus be concerned by physical quantities obtained after averaging over the whole flow domain. Using

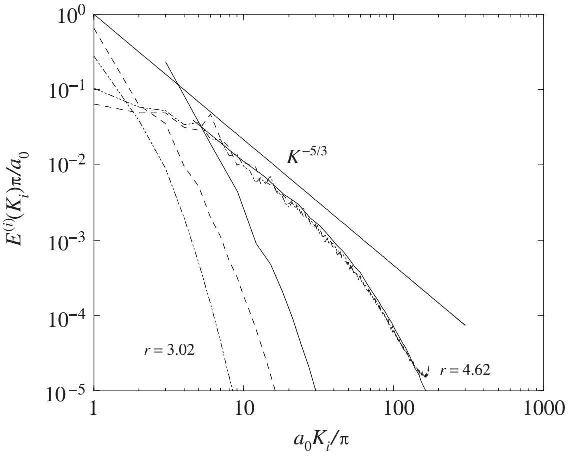

Figure 19. Spectral density of kinetic energy $E^{(1)}(K_1)$ (——), $E^{(2)}(K_2)$ (- - -) and $E^{(3)}(K_3)$ (·····) as functions of K_1, K_2, K_3, components of the wavevector. Spectral DNS results.

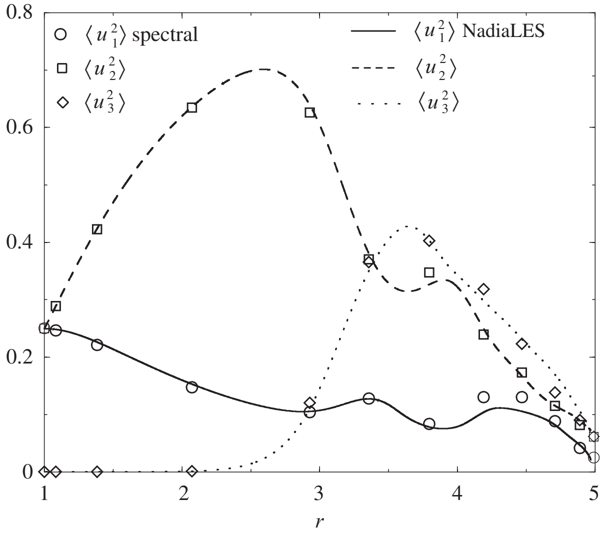

Figure 20. Spatial averages of the squared velocity components vs compression ratio $r(t)$: NadiaLES: $\alpha = 0.025$, dynamic Smagorinsky model: $\langle u_1^2\rangle$, —— ; $\langle u_2^2\rangle$, - - - - ; $\langle u_3^2\rangle$, ... Spectral: $\langle u_1^2\rangle$, ○; $\langle u_2^2\rangle$, □; $\langle u_3^2\rangle$, ◇.

the symbol $\langle\rangle$ for averages over the flow domain, the variations of $\langle u_i^2\rangle$ have been plotted in Figure 20. The sum of the three components (twice the kinetic energy per unit mass), is also presented in Figure 21. Continuous lines indicate LES predictions and symbols are used for the filtered DNS results.

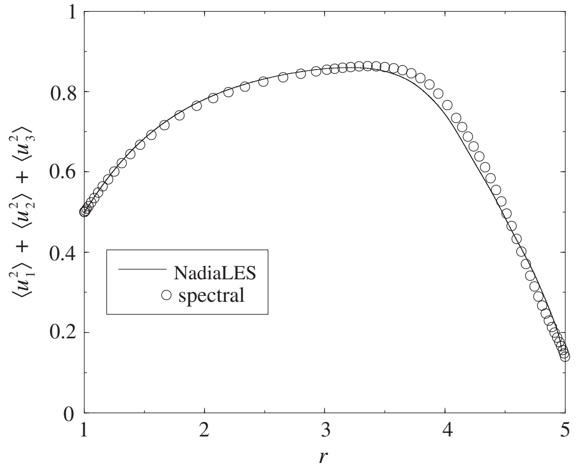

Figure 21. Evolution of $\langle u_1^2\rangle + \langle u_2^2\rangle + \langle u_3^2\rangle$ as function of compression ratio $r(t)$. NadiaLES: $\alpha = 0.025$, dynamic Smagorinsky model.

The compression is responsible for the increase of the flow kinetic energy. The maximum is observed near $r = 4$. After that, the role of dissipation, enhanced by turbulent transfers to small scales, is prevailing and the kinetic energy rapidly decreases. Three phases can be identified. From $r = 1$ to 2.25, the effect of the perturbation is not significant and the flow remains two-dimensional. The respective decrease and increase of u_1 and u_2 are the consequences of the vortex flattening. From $r = 2.25$ to 3.75, the instability is characterized by an increase of the u_3 component. Compared to the 2D non-perturbated analytical solution, the total kinetic energy appears not to be affected by the perturbation during this period of time. The dissipation due to instability and turbulent generation becomes increasingly dominant in the late compression.

As seen in Figures 20 and 21, the LES predictions are in a satisfactory agreement with the direct spectral simulation. The total kinetic energy is however slightly overestimated at the end of the compression due to an excess of the u_3 contribution.

To make the role of α explicit, the time variations of $\langle u_k u_k\rangle$ obtained using the different values $\alpha =$ 0.025, 0.05, 0.1 are plotted in Figure 22. The same dynamic Smagorinsky model is used for the three simulations. In the initial phase till $r = 3.5$, the results are clearly not influenced by α. Then, the effect of a too large value of α is to reduce the level of kinetic energy. The numerical dissipation terms [11] are formed by fourth-order space derivatives which have a larger damping effects on high frequencies, explaining why the numerical viscosity acts more at the end of the compression when small structures are dominant. The best results are here obtained for $\alpha = 0.025$.

Keeping the value $\alpha = 0.025$, the results from the standard and dynamic Smagorinsky models are compared in Figure 23. Simulations were also attempted without using a subgrid model, leading to an observed loss of numerical stability for values of α lower than 0.05. Compared to the dynamic model, the standard Smagorinsky model is clearly too diffusive especially in the laminar period from $r = 3.5$ and in the turbulent phase till $r = 4.5$. At the end of the compression, both models give comparable energy levels.

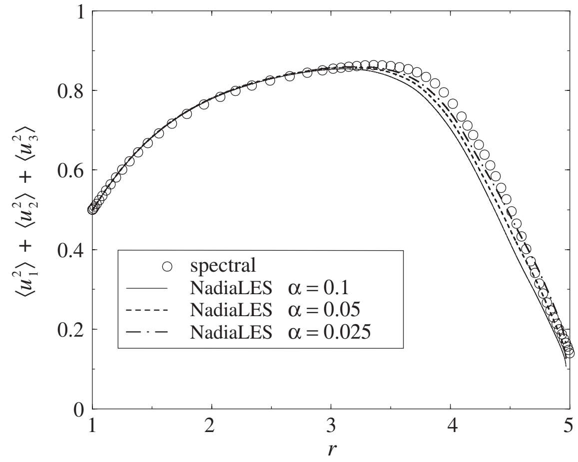

Figure 22. Evolution of $\langle u_1^2\rangle + \langle u_2^2\rangle + \langle u_3^2\rangle$ as function of compression ratio $r(t)$. NadiaLES: $\alpha = 0.1$, 0.05, 0.025, dynamic Smagorinsky model.

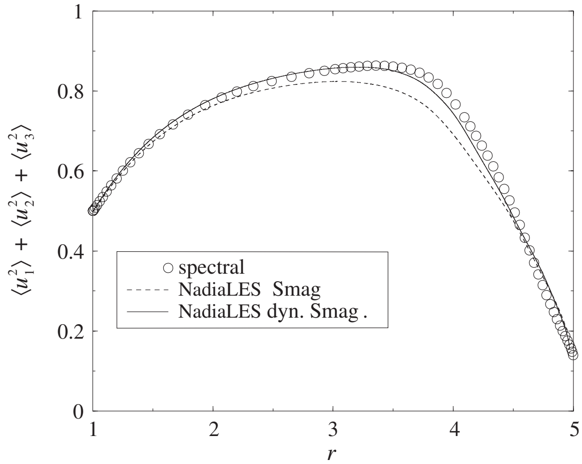

Figure 23. Evolution of $\langle u_1^2\rangle + \langle u_2^2\rangle + \langle u_3^2\rangle$ as function of compression ratio $r(t)$. NadiaLES: $\alpha = 0.025$, standard and dynamic Smagorinsky model.

The evolution of the subgrid viscosity, non-dimensionalized by the laminar viscosity, is presented in Figure 24. For both models, the subgrid viscosity μ_t grows until $r = 4$ because of the increase of mean strain magnitude $|\overline{S}|$ and then slightly decreases between $r = 4$ and 5. The variations with α are such that μ_t decreases with a larger amount of numerical viscosity. It must also be noted that the standard Smagorinsky model predicts larger values of μ_t during the first part of the compression. Overprediction is due to the fact the value of the constant C_s is clearly not appropriate to this phase of the flow evolution which is essentially laminar.

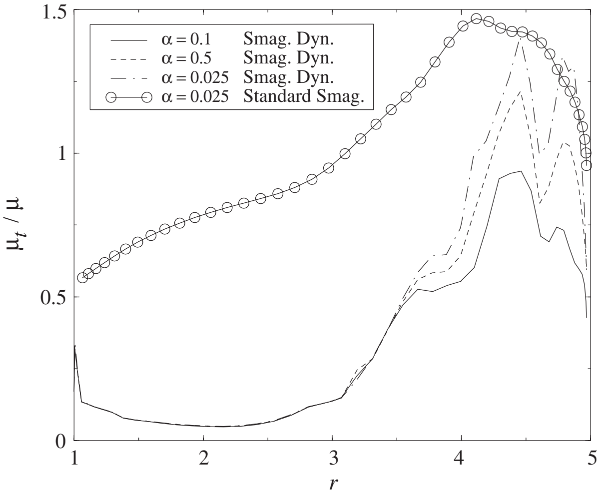

Figure 24. Evolution of the subgrid-scale viscosity μ_t as function of compression ratio $r(t)$.

The main advantage of the dynamic model is in allowing the constant to self-adapt to the flow conditions. As can be seen in Figure 24, the dynamically adapted coefficient remains moderate during the laminar phase and the values μ_t remains substantially lower.

5. CONCLUSION

This paper investigates the ability of LES and second-order numerical method on unstructured meshes to simulate a Taylor vortex submitted to a compression. The studied test case is a simplified model of the tumble flow encountered inside internal combustion chambers. The numerical solver uses a mixed FV/FE approximation on unstructured meshes with second-order accuracy. Combined with LES subgrid-scale models, satisfactory results have been obtained in two test cases: decaying homogeneous isotropic turbulence and the compressed Taylor vortex. These results are encouraging in the perspective of application to more complex problems: one example is the tumbling flow inside a compression chamber [8].

One drawback of second-order upwind schemes, such as the one used in this paper, is its possible excessive numerical dissipation. For the present method, the numerical dissipation is controlled by a parameter α that must be as low as possible to avoid too large dissipation at the small scales, while keeping high enough values to avoid numerical instabilities. For the studied test cases, the value $\alpha = 0.025$ seems to be close to the optimum. It should be noted however that, for the present turbulent simulations, the predicted kinetic energy levels are not critically dependent on the precise value of α. The reason is that the subgrid-scale model dissipation is shown to adapt itself to the level of numerical dissipation. Increasing α by a factor of 4 makes the subgrid-scale viscosity μ_t decrease by a factor 1.7 (Figure 9), but affects the kinetic energy levels only by a decrease of less than 10% (Figure 5). Compared to the standard Smagorinsky subgrid model, the dynamic formulation improves this observed compensation for the two test cases. To make the results less dependent on the value of α, a higher order MUSCL interpolation could be used, as the one developed by Camarri *et al.* [31], this method leads however to a doubling of the computational cost.

Finally, it is also demonstrated that the dynamic Smagorinsky model is superior to the standard one in predicting the laminar-turbulent transition occuring in the Taylor vortex.

ACKNOWLEDGEMENTS

This work was developed as a part of ARC 'Moteurs propres et économes' supported by the CNRS, PSA and Renault. Computer time was provided by the Centre Informatique National de l'Enseignement Supérieur at Montpellier. The authors would like to thank Anne Cadiou, research engineer at the LMFA, for her great help in developing the numerical tests.

REFERENCES

1. Lesieur M, Métais O. New trends in large-eddy simulations of turbulence. *Annual Review of Fluid Mechanics* 1996; **28**:45–82.
2. Pope B. *Turbulent Flows*. Cambridge University Press: Cambridge, 2000.
3. Méneveau C, Katz J. Scale-invariance and turbulence models for large-eddy simulations. *Annual Review of Fluid Mechanics* 2000; **32**:1.
4. Sagaut P. *Large Eddy Simulations or Incompressible Flows* (2nd edn). Springer: Berlin, 2002.
5. Marc D, Borée J, Bazile R, Charnay G. Combined PIV and LDV analysis of the evolution and breakdown of a compressed tumbling vortex. *11th Symposium on Turbulent Shear Flows*, Grenoble, 1997.
6. Borée J, Maurel S, Bazile R. Disruption of a compressed vortex. *Physics of Fluids* 2002; **14**(7).
7. Le Roy O, Le Penven L. Compression of a turbulent vortex flow. *International Journal of Heat and Fluid Flow* 1998; **19**:533–540.
8. Toledo M, Le Penven L, Buffat M, Cadiou A. LES of a compressed turbulent vortex flow. *10th European Turbulence Conference*, 29 June–02 July 2004, Trondheim, Norway, 2004.
9. Jansen KE. Large-eddy simulations of flow around a NACA 4412 aerofoil using unstructured grids. *CTR Annual Research Briefs*, 1996.
10. Bui T. A parallel finite-volume algorithm for large-eddy simulation of turbulent flows. *Computers and Fluids* 2000; **29**:877–915.
11. Camarri S, Salvetti MV, Koobus B, Dervieux A. Large-eddy simulation of a bluff-body flow on unstructured grids. *International Journal for Numerical Methods in Fluids* 2002; **40**:1431–1460.
12. Mahesh K, Contantinescu G, Moin P. A numerical method for large-eddy simulation in complex geometries. *Journal of Computational Physics* 2004; **197**:215–240.
13. Haworth DC, Jansen KE. Large-eddy simulation on unstructured deforming meshes: towards reciprocating IC engines. *Computers and Fluids* 2000; **29**:493–524.
14. Moureau V, Barton I, Angelberger Ch, Poinsot T. Towards large-eddy simulation in internal-combustion engines: simulation of a compressed tumble flow. *SAE Paper 2004-01-1995*, 2004.
15. Vreman AW. Direct and large-eddy simulation of the compressible turbulent mixing layer. *Ph.D. Thesis*, University of Twente Enschede, 1995.
16. Smagorinsky J. General circulation experiments with the primitive equations. *Monthly Weather Review* 1963; **91**:99–164.
17. Erlebacher G, Hussaini MY, Speziale CG, Zang TA. Toward the large-eddy simulation of compressible flows. *Journal of Fluid Mechanics* 1992; **238**:155–185.
18. Germano M, Piomelli U, Moin P, Cabot WH. A dynamic subgrid-scale eddy viscosity model. *Physics of Fluids A* 1991; **3**(7):1760–1765.
19. Dervieux A. Steady Euler simulations using unstructured meshes. *VKI*, *Lectures Series* 1984–04, 1985.
20. Duchamp L. Simulation des grandes échelles d'écoulements compressibles et réactifs sur maillage non-structuré. *Thèse de doctorat*, Ecole Centrale de Lyon, 1999.
21. Roe PL. A numerical method for solving the equations of compressible viscous flows. *AIAA Journal* 1982; **20**(9):1275–1281.
22. Van Leer B. Flux vector splitting for the Euler equations. *Lecture Notes in Physics* 1982; **170**:405–512.
23. Carpentier R. Comparison entre des schémas 2D de type Roe sur maillage régulier triangle ou quadrangle. *INRIA Report 3360*, 1998.
24. Guillard H, Viozat C. On the behavior of upwind schemes in the low Mach number limit. *Computers and Fluids* 1999; **28**:63–86.

25. Turkel E. Review of preconditioning methods for fluid dynamics. *Applied Numerical Mathematics* 1993; **12**:257–284.
26. Viozat C. Implicit upwind scheme for low Mach number compressible flows. *INRIA Report 3084*, 1997.
27. Comte-Bellot G, Corrsin S. Simple Eulerian time correlation of full and narrow-band velocity signals in grid-generated 'isotropic' turbulence. *Journal of Fluid Mechanics* 1971; **48**:273–337.
28. Lundgren TS, Mansour NM. Transition to turbulence in an elliptic vortex. *Journal of Fluid Mechanics* 1996; **307**:43–62.
29. Sipp J, Jacquin L. Elliptic instability in two-dimensional flattened Taylor–Green vortices. *Physics of Fluids* 1998; **10**(4):839–849.
30. Le Roy O. *Thèse de doctorat*, Ecole Centrale de Lyon, 1998.
31. Camarri S, Salvetti MV, Koobus B, Dervieux A. A low-diffusion MUSCL scheme for LES on unstructured grids. *Computers and Fluids* 2004; **33**:1101–1129.